The Radio Parallax of the Crab Pulsar: A First VLBI Measurement Calibrated with Giant Pulses

The Astrophysical Journal, 952:161 (13pp), 2023 August 1 https://doi.org/10.3847/1538-4357/acdc98

The Radio Parallax of the Crab Pulsar: A First VLBI Measurement Calibrated with Giant Pulses

Rebecca Lin[1], Marten H. van Kerkwijk[1], Franz Kirsten[2], Ue-Li Pen[3,4,5,6,7], and Adam T. Deller[8,9]
[1] Department of Astronomy and Astrophysics, University of Toronto, 50 St. George Street, Toronto, ON M5S 3H4, Canada; lin@astro.utoronto.ca
[2] Department of Space, Earth and Environment, Chalmers University of Technology, Onsala Space Observatory, SE-439 92, Onsala, Sweden
[3] Institute of Astronomy and Astrophysics, Academia Sinica, Astronomy-Mathematics Building, No. 1, Section 4, Roosevelt Road, Taipei 10617, Taiwan
[4] Canadian Institute for Theoretical Astrophysics, 60 St. George Street, Toronto, ON M5S 3H8, Canada
[5] Canadian Institute for Advanced Research, 180 Dundas Street West, Toronto, ON M5G 1Z8, Canada
[6] Dunlap Institute for Astronomy and Astrophysics, University of Toronto, 50 St George Street, Toronto, ON M5S 3H4, Canada
[7] Perimeter Institute of Theoretical Physics, 31 Caroline Street North, Waterloo, ON N2L 2Y5, Canada
[8] Centre for Astrophysics and Supercomputing, Swinburne University of Technology, John Street, Hawthorn, VIC S1RR, Australia
[9] ARC Centre of Excellence for Gravitational Wave Discovery (OzGrav), Australia
Received 2023 June 2; revised 2023 June 5; accepted 2023 June 6; published 2023 July 27

Abstract

We use four observations with the European very long baseline interferometry (VLBI) network to measure the first precise radio parallax of the Crab Pulsar. We found two in-beam extragalactic sources just outside the Crab Nebula, with one bright enough to use as a background reference source in our data. We use the Crab Pulsar's giant pulses to determine fringe and bandpass calibration solutions, which greatly improved the sensitivity and reliability of our images and allowed us to determine precise positional offsets between the pulsar and the background source. From those offsets, we determine a parallax of $\pi = 0.53 \pm 0.06$ mas and proper motion of $(\mu_\alpha, \mu_\delta) = (-11.34 \pm 0.06,\ 2.65 \pm 0.14)$ mas yr^{-1}, yielding a distance of $d = 1.90^{+0.22}_{-0.18}$ kpc and transverse velocity of $v_\perp = 104^{+13}_{-11}$ km s^{-1}. These results are consistent with the Gaia 3 measurements, and open up the possibility of far more accurate astrometry with further VLBI observations.

Unified Astronomy Thesaurus concepts: Very long baseline interferometry (1769); Supernova remnants (1667); Radio bursts (1339); Radio astrometry (1337); Pulsars (1306); Parallax (1197)

1. Introduction

The Crab Pulsar (PSR B0531+21) is one of the youngest pulsars, situated at the heart of the Crab Nebula, the remnant of supernova SN 1054 (Duyvendak 1942; Mayall & Oort 1942). One of the most observed pulsars, it has been continuously monitored by the 13 m dish at the Jodrell Bank Observatory since 1984 (Lyne et al. 1993). The mean radio profile of the pulsar shows multiple components, with the dominant ones being the main pulse (MP) and interpulses (IPs), which are made up of "giant pulses," extremely narrow and bright pulses (for a review, see Eilek & Hankins 2016). The pulse emissions are not only bright in radio but visible up to γ-ray energies with the MP and IPs showing strong alignment across the full electromagnetic spectrum (Moffett & Hankins 1996). The pulsar also undergoes glitches, discrete changes in the pulsar rotation rate, every few years[10] (e.g., Espinoza et al. 2011; Shaw et al. 2021). This wealth of pulse phenomena offers a great opportunity for understanding the pulsar emission mechanism and possibly constraining the nuclear physics of neutron star interiors. Additionally, the young age of this system (~1000 yr) makes it the ideal laboratory to study not only the evolution of young pulsars but also pulsar wind nebulae and supernova remnants.

Since the discovery of the Crab Pulsar, there have been several attempts to constrain the distance and proper motion of the pulsar. For the distance, early attempts based on various lines of evidence including kinematic, spectroscopic, and age-related considerations placed the pulsar between 1.4 and 2.7 kpc (Trimble 1973). From galactic electron density distribution models, the distance to the pulsar can be estimated as ~1.7 kpc with the NE2001 model (Cordes & Lazio 2002) and ~1.3 kpc with the YMW16 model (Yao et al. 2017).

While these estimates give a sense of the distance, none of them are precise and none are direct measurements. Indeed, many rely on assumptions one would like to test. For instance, the kinematic constraints implicitly assume a roughly spherical nebula, while the dispersion-measure-based distances rely on electron density models.

For the proper motion, similarly early measurements of the Crab Pulsar were relatively poor (Minkowski 1970; Wyckoff & Murray 1977; Caraveo & Mignani 1999). A first relatively precise measurement was derived from Hubble Space Telescope observations spanning over a decade, of $(\mu_\alpha, \mu_\delta) = (-11.8 \pm 0.4 \pm 0.5,\ \ 4.4 \pm 0.4 \pm 0.5)$ mas yr^{-1} (Kaplan et al. 2008).

While a precise parallax and proper-motion measurement of the Crab Pulsar would be important, it is impeded by complications in doing astrometry at both radio and optical wavelengths; furthermore, due to the glitches, pulsar timing also cannot help (for a review, see Kaplan et al. 2008). In the optical, this changed with the Gaia mission, which presented the first precise astrometry in its second data release (Gaia DR2; Gaia Collaboration et al. 2018): $\pi = 0.27 \pm 0.12$ mas and $(\mu_\alpha,\ \mu_\delta) = (-11.8 \pm 0.2,\ 2.65 \pm 0.17)$ mas yr^{-1}, respectively. The precision was improved in the third data release, Gaia DR3 (Antoniadis 2020; Gaia Collaboration et al. 2023): $\pi = 0.51 \pm 0.08$ mas and $(\mu_\alpha, \mu_\delta) = (-11.51 \pm 0.10,\ 2.30 \pm 0.06)$ mas yr^{-1}, respectively.

[10] http://www.jb.man.ac.uk/pulsar/glitches.html

Table 1
Observation and Giant Pulse Log

Observation Code	Date	MJD	t_{exp}[a] (h)	t_{target}[b] (h)	Telescopes Used[c]	DM[d] (pc cm^{-3})	Giant Pulses[e]	
							N	r (min^{-1})
EK036 A	2015 Oct 18	57313.96	4	3.27	Ef Bd Hh Jb Mc O8 Ro* Sv T6* Tr Wb Zc	56.7772	686	3.50
EK036 B	2016 Oct 31	57692.98	2	1.65	Ef Bd Hh Mc O8 Sv Wb Zc	56.7668	1067	10.81
EK036 C	2017 Feb 25	57809.67	2	1.15	Ef Bd Hh Jb Mc O8 Sv Ur Wb Zc	56.7725	281	4.08
EK036 D	2017 May 28	57901.40	2	1.24	Ef Bd Hh Jb-II Mc O8 Sv Tr Ur Wb Zc	56.7851	740	9.94

Notes.
[a] Total observing time, including telescope setup and calibration.
[b] Total exposure on target.
[c] We omit telescopes where data were corrupt, where significant radio frequency interference (RFI) occurred and/or where we were unable to determine reliable fringe solutions. Asterisks beside a telescope indicate that the telescope was unable to see the source for the full observing time; furthermore, Ro had left-circular polarization only. Abbreviations are: Ef: the 100 m Effelsberg telescope; Bd: the 32 m at Badary; Hh: the 26 m in Hartebeesthoek; Jb: the 76 m Lovell telescope; Jb-II: the 25 m Mark II Telescope at the Jodrell Bank Observatory; Mc: the 32 m at Medicina; O8: the 25 m at Onsala; Ro: the 70 m at the Robledo Deep Space Station; Sv: the 32 m at Svetloe; T6: 65 m at Tianma; Tr: the 32 m at Toruń; Wb: the 25 m RT1 telescope at Westerbork; and Zc: the 32 m at Zelenchukskaya.
[d] Inferred from the giant pulses.
[e] Total number and rate of giant pulses (including both MP and IP) found using a detection threshold of 50σ on incoherently summed data (for details, see Lin et al. 2023).

While impressive, the difference in measured parallax between the two data releases is somewhat worrying. It might be related to the fact that the measurements are affected by the Crab Pulsar not being a typical optical source, being embedded in an optically bright nebula and producing variable emission near itself that would be only marginally resolved. Hence, it would be best to have an independent measurement.

At radio wavelengths, very long baseline interferometry (VLBI) has been very successful in measuring accurate parallaxes and proper motions for pulsars both weaker and farther away than the Crab Pulsar (e.g., Chatterjee et al. 2009; Deller et al. 2019). For the Crab Pulsar, a difficulty is that it is embedded in a large, $\sim 6' \times 4'$, radio-bright nebula. The high brightness effectively raises the overall system temperature in any observation, making the average emission of the Crab Pulsar hard to detect. This particularly affects observations at higher frequencies, where the angular resolution is better but the pulse emission is fainter ($f_\nu \propto \nu^{-3.1}$, Lorimer et al. 1995). But at lower frequencies, where the pulsar is brighter, the ionosphere hinders astrometry, especially in the absence of an extragalactic source that can be used as an in-beam calibrator—which has to be outside the nebula, since otherwise it would be severely broadened by scattering.

The problem of a lack of an in-beam calibrator has recently been solved: the Wide-field VLBA Calibrator Survey (WFCS; Petrov 2021) lists a suitable nearby source (one that we also discovered independently; see Section 2). With such an in-beam extragalactic source, one avoids uncertainties in extrapolating phasing solutions for a phase calibrator that is multiple degrees away. And even if the in-beam calibrator is not very bright, a parallax measurement to within a 0.1 mas should be possible if one can self-calibrate on the pulsar (Fomalont et al. 1999; Deller et al. 2019).

For the Crab Pulsar, the bright nebula prevents self-calibration on the regular pulse emission (e.g., Lobanov et al. 2011 used an external phase calibrator for their VLBI imaging). In principle, the Crab Pulsar's giant pulses can help, as they are extremely bright and can be detected with single dishes. Because they occur randomly in time, however, even pulsar gating on the corresponding phase windows does not give very good signal-to-noise ratios (S/Ns).

In this paper, we present a technique using only the Crab Pulsar's giant pulses to model ionospheric and instrumentation variations for self-calibration, and show that with the newly found nearby extragalactic reference sources this enables precise parallax and proper-motion measurements. In the following, we first describe in Section 2 the VLBI data we took, as well as the archival Very Large Array (VLA) data set we used to search for extragalactic references. In Section 3, we describe how we correlated our VLBI data to form visibilities, calibrated the visibility data with the giant pulses, and extracted positions of our sources. In Section 4, we derive the parallax and proper motion from the positions. We compare with the Gaia results in Section 5, and discuss ramifications and future prospects in Section 6.

2. Observations

Our observations were taken with the European VLBI Network (EVN) at four epochs between 2015 October and 2017 May, using a total of 10 hr (see Table 1). Real-sampled data in left and right circular polarizations were recorded in either 2 bit MARK 5B or VDIF format at each telescope, except for the 70 m at the Robledo Deep Space Station (Ro) where only left circular was available. The frequency range of 1594.49–1722.49 MHz was covered, in either eight contiguous 16 MHz or four contiguous 32 MHz wide bands.

Individual scans on the Crab Pulsar lasted ~5 (EK036 C-D) to ~25 minutes (EK036 A-B), and were interleaved with observations of J0530+1331 (~5 to ~10 minutes, bandpass calibrator source at 8.°5 from the target) and/or J0518+2054 (~0.5 to ~1 minutes, phase calibrator source at 4.°0 from the target). The unusually long integration times on the target (in particular in EK036 A and B) and short integrations on the phase calibrator were chosen because we only intended the phase calibrator to provide a first crude calibration, just enough to later perform self-calibration on the target; we realized phase calibration at the level required for accurate astrometry would be impossible given the large separation between target and phase calibrator and the bright emission from the Crab Nebula.

After a first inspection of the data from EK036 A, however, it became clear that our initial approach led to phase errors that

Table 2
Target and Calibrator Scan Pointing Centers

Source	R.A. (α)	Decl. (δ)	Sep. (°)
PSR B0531+21	$05^h34^m31\overset{s}{.}934$	$22°00'52\overset{''}{.}191$	...
J0530+1331	$05^h30^m56\overset{s}{.}4167465$	$13°31'55\overset{''}{.}149516$	8.5
J0518+2054	$05^h18^m03\overset{s}{.}8245128$	$20°54'52\overset{''}{.}497365$	4.0

Note. Coordinates listed here are in the J2000 FK5 frame. The separation between the calibrator sources and the Crab Pulsar is given in the last column.

were too large to perform traditional self-calibration on the Crab Pulsar (see Figure 4). Hence, we reduced the integration times on the target in the subsequent EK036 C and D observations (e.g., Lobanov et al. 2011 were able to transfer phase solutions from J0518+2054 using a much shorter calibrator/target cycle of 2/5 minutes.).

At the time of these observations, no extragalactic sources near the Crab Pulsar were known that would be suitable as in-beam calibrators. Therefore, the Crab Pulsar pointings were centered on the pulsar itself (see Table 2), in the hope that suitable in-beam references could be found within the field of view of the smaller participating stations.

Given the high resolution of the EVN data, an untargeted search for in-beam sources is nearly intractable. Instead, we searched for candidates in an archival VLA data set (project code 12B-380), taken in A-array configuration on 2012 November 26 and 27 at 3 GHz (*S* band, covering 2–4 GHz). We used the standard Common Astronomy Software Applications VLA calibration pipeline (CASA 5.1.1; The CASA Team et al. 2022) to perform automatic flagging and calibration of the two data sets. No careful flux calibration was applied. After inspection of the data, we decided to focus only on the later run, from 2012 November 27. We used the CASA task `tclean` for imaging, limiting ourselves to the lower half of the frequency band, i.e., 2–3 GHz. Moreover, we limited the *uv* range, excluding visibilities from baselines $<75\,k\lambda$ in order to filter out the extended emission from the Crab Nebula itself. Since our aim was to find compact sources within the field of view of the VLA, we generate an image of 8192×8192 pixels at an angular resolution of $0\overset{''}{.}15\,\mathrm{pixel}^{-1}$, oversampling by about a factor 3 the 477×470 mas beam (position angle $-60°$). The rms in the final image varies by a factor of up to 4 between the central region and the outer region of the image because of the Crab Nebula's emission.

We exported the cleaned image as an FITS file and searched for radio sources by normalizing the image relative to a median-filtered version to pick out outliers. In this way, we found 10 candidates, which we list in Table 3 and show in Figure 1.

For all of the candidates, we created images from our EVN data, finding that the two brightest ones were detected: SE_CAND3 and NE_CAND4 (see Section 3.3 and Figure 5). We were able to find a source at the location of SE_CAND3 in the new Wide Field Very Long Baseline Array (VLBA) calibrator survey (Petrov 2021), which lists it as the compact source WFCS J0535+2156, and in the VLA Sky Survey (VLASS; Gordon et al. 2021) as VLASS1QLCIR J053506.32+215649.3. Candidate NE_CAND4 was also seen in VLASS as VLASS1QLCIR J053514.04+220407.7, but not in the VLBA catalog.

Looking through other catalogs, we found sources matching the position of SE_CAND3 in the Wide-field Infrared Survey Explorer Data Release (Cutri et al. 2012) and in the UKIRT Infrared Deep Sky Survey (Lawrence et al. 2012). It also has a counterpart in Gaia DR3 (Gaia Collaboration et al. 2023), with a parallax and proper motion consistent with zero. Thus, it seems likely that SE_CAND3 is an active galactic nucleus.

Table 3
Candidate Extragalactic Sources from VLA Data

Source	R.A. (α)	Decl. (δ)	Peak S/N[a]	Sep. (′)
NE_CAND1	$05^h34^m50\overset{s}{.}43$	$22°03'37\overset{''}{.}58$	16.3	5.1
NE_CAND2	$05^h34^m50\overset{s}{.}93$	$22°06'39\overset{''}{.}79$	8.4	7.3
NE_CAND3	$05^h34^m50\overset{s}{.}80$	$22°04'46\overset{''}{.}41$	4.9	5.9
NE_CAND4	$05^h35^m14\overset{s}{.}05$	$22°04'07\overset{''}{.}43$	42.6	10.3
SE_CAND1	$05^h34^m55\overset{s}{.}31$	$21°55'18\overset{''}{.}94$	14.8	7.8
SE_CAND2	$05^h34^m40\overset{s}{.}74$	$21°55'15\overset{''}{.}31$	6.5	6.0
SE_CAND3	$05^h35^m06\overset{s}{.}34$	$21°56'49\overset{''}{.}11$	463.0	8.9
NW_CAND1	$05^h34^m07\overset{s}{.}34$	$22°08'45\overset{''}{.}63$	19.8	9.7
SW_CAND1	$05^h34^m11\overset{s}{.}62$	$21°58'53\overset{''}{.}38$	18.7	5.1
SW_CAND2	$05^h34^m15\overset{s}{.}14$	$21°57'12\overset{''}{.}71$	14.0	5.3

Note. Coordinates listed here are in the J2000 FK5 frame. SE_CAND3 and NE_CAND4 where later confirmed to be visible in the EVN data. The separation between the candidate sources and the Crab Pulsar is given in the last column.
[a] As found in the VLA data.

3. Correlation, Calibration, Images, Positions, and Uncertainties

3.1. Visibilities

We correlated the data from the different telescopes using the publicly available Super FX Correlator (SFXC 5.1; Keimpema et al. 2015), which, prior to performing the correlations, corrects for station clock offsets and rates, as well as for geometric delays using CALC10[11] (Ryan & Vandenberg 1980). At this stage, no additional station-specific delays or atmospheric distortions of the wave front are taken into account.

For each observation, two correlation passes were performed. The first pass correlated on the Crab Pulsar in pulsar gating mode (described below), and on the bandpass and phase calibrators in ungated mode. The correlation centers in this pass are the same as the antenna pointing centers given in Table 2. In the second correlator pass, we correlated all target scans again, but now ungated and centered on the locations of our candidate sources (see Table 3), using SFXC's multiphase center mode.

For the pulsar gating, we created polyco files using TEMPO2 (Hobbs & Edwards 2012) with the Crab Pulsar ephemeris, starting from the ephemeris provided by Jodrell Bank Observatory[12] (Lyne et al. 1993) and then adjusting the phase and dispersion measure to values found in Lin et al. (2023) for the same data (see Table 1). With these, we used SFXC to incoherently de-disperse,[13] fold, and gate the pulsar

[11] https://space-geodesy.nasa.gov/techniques/tools/calc_solve/calc_solve.html
[12] http://www.jb.man.ac.uk/~pulsar/crab.html
[13] SFXC version 5.1 does not have coherent de-dispersion capabilities.

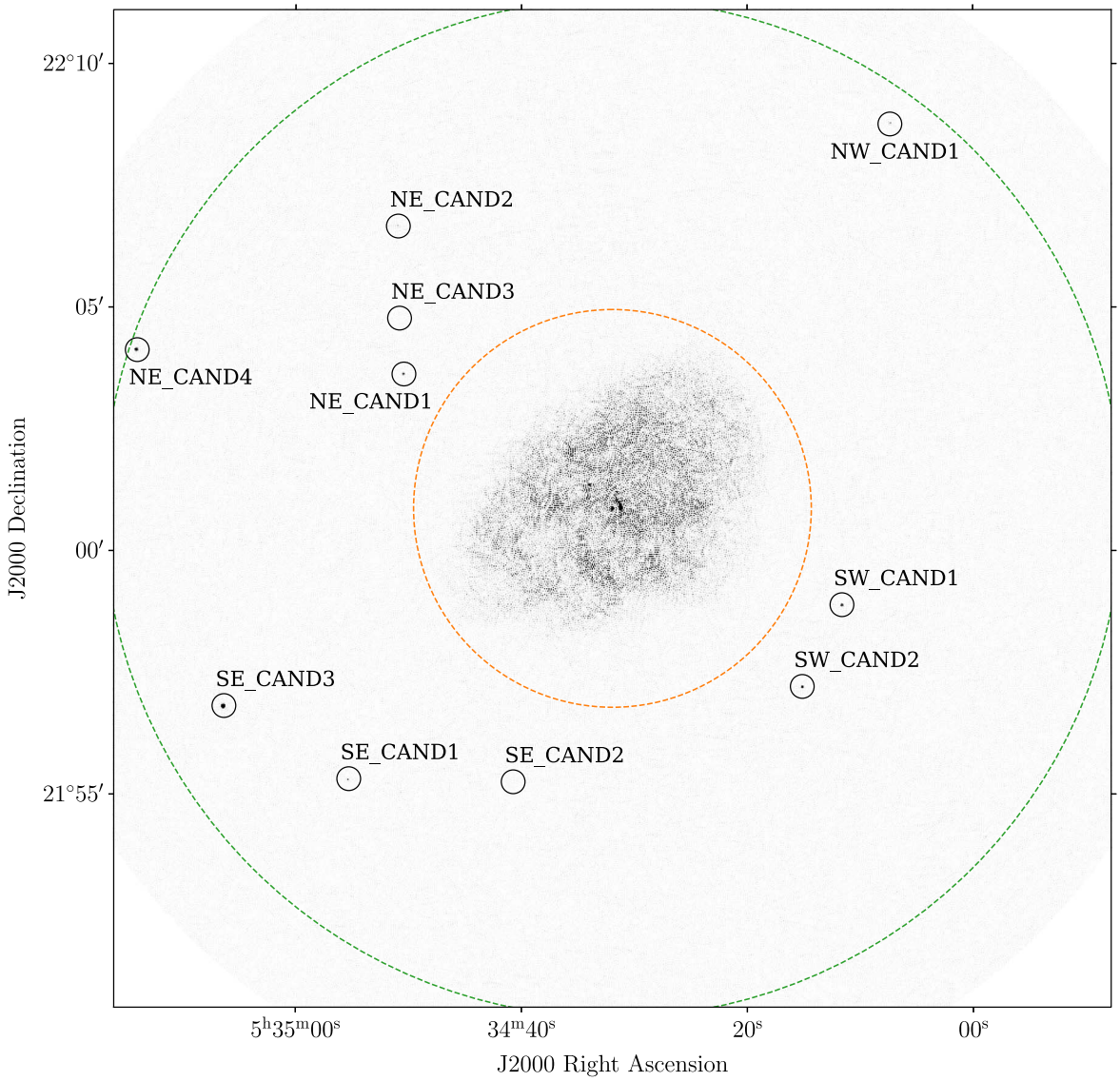

Figure 1. VLA image of the Crab Pulsar with our 10 candidate reference sources marked (black circles). Overlaid are the approximate fields of view of Effelsberg (orange dotted circle) and Badary (green dotted circle), as implied by the FWHM at our central observing frequency (using effective apertures of 78 m and 30.5 m, respectively). All candidates are outside the field of view of Effelsberg, but within the fields of view of most other dishes, which have diameters comparable to Badary.

observations on the MP phase window (2.1% of the ∼33 ms pulse period).

With the gated mode, we gain S/N by removing time ranges when little if any pulsar signal is present. However, since giant pulses are short in duration (most of the signal is within the scattering timescale of ∼5 μs at our observing frequency; see Lin et al. 2023 for examples of giant pulses from these data sets) and occur only in some pulse rotations, one could in principle get a much better S/N by only including pulse rotations in which giant pulses occur. Furthermore, one could also include IP giant pulses and possibly other pulse components. We did not pursue these potential improvements, since we find below (in Section 3.3) that the S/N of the images created from the MP gated visibilities is much larger than that of the in-beam candidate sources, and thus does not limit the accuracy of the astrometry.

For all correlations, we used a spectral resolution of 4096 channels across the total bandwidth, limiting any dispersive in-channel smearing to 3 μs (of order a giant pulse width). We used a temporal resolution of 0.5 s to have the option of, in post-processing, selecting only time integrations where particularly bright giant pulses occurred (but we did not use this, as the S/N sufficed). In total, for each observation, 11 visibility sets were created, one for the Crab Pulsar and one each for our candidate sources. Calibrator visibility data were included in each visibility set; hence, each set contained three sources.

3.2. Calibration

We calibrated our visibilities with the help of CASA 6.5, writing custom calibration scripts to ensure that our calibrations are consistent across all observations and to help track our configurations.

In preparation, we first converted visibility data to CASA Measurement Sets using Joint Institute for VLBI in Europe

(JIVE) post-processing tools, and set up antenna tables with diameters and axis offsets from the station summary files. We also set up amplitude calibration tables with system temperature, gain curve, and primary beam corrections. Since system temperature and gain curve measurements from the telescope logs were affected by the bright Crab Nebula and thus unreliable (and some were simply missing), we instead used nominal values taken from the EVN status table[14] and included the flux density of the Crab Nebula $S_{\rm CN} = 955\nu^{-0.27}$ Jy, where ν is our observing frequency in gigahertz (Bietenholz et al. 1997). As our goal is precise astrometry, the true flux density of our sources is of little importance, and this flux scaling is sufficient for estimating which of the candidate sources will likely be visible in the EVN data sets. We flagged times and frequencies where the signal was poor (i.e., before the start and end of each scan, and at passband edges), as well as particularly strong radio frequency interference (RFI) previously detected in the baseband data (see Lin et al. 2023), taking care to ensure that giant pulse signals were not accidentally removed. Finally, to account for the reduced sensitivity away from the antenna pointings, we applied a primary beam correction for our in-beam candidate correlation centers (assuming an Airy disk with effective aperture sizes provided by the JIVE team, separately for each of our eight spectral windows).

For calibration, we started by determining phase and delay corrections due to instrument and atmospheric variations toward our calibrator sources: we use CASA's `fringefit` task to determine solutions in 60 s intervals for each spectral window and polarization independently, with Effelsberg as the reference antenna. We attempted transferring the fringe solutions to the Crab Pulsar, but found relatively poor results (see Figure 4 and Section 3.3 below). This was not unexpected given that our calibrators are far from the Crab Pulsar and that the target scans are relatively long compared to the timescale of a few minutes of ionospheric variations.

Since the Crab Pulsar is the brightest of the in-beam sources, we instead used it to self-calibrate. We first tried using the gated pulsar visibilities from SFXC, but these do not have sufficient S/Ns on short integrations, and hence the resulting fringe solutions obtained using CASA's `fringefit` task were unreliable, showing extreme variations without any discernible pattern.

Instead, we follow Lin et al. (2023) and use giant pulses to model the delays, amplitude, and phase rotations in each spectral window, and write these models to CASA compatible fringe and amplitude tables. Specifically, we use all giant pulses (both MP and IP) detected with an S/N of 50 in the incoherently summed telescope data (a cutoff that ensures no false detections; we find no pulses outside of the MP and IP phase windows; see Lin et al. 2023 for details on the data reduction giant and giant pulse detection). We show an example of an extreme fringe solution in Figure 2 (for Badary in the EK036 A observation, where the Crab Pulsar is setting, causing a rapid increase in path length through the ionosphere and thus a large increase in fringe rate). We applied these solutions to both the Crab Pulsar and the candidate in-beam source visibility sets.

Since our detection rate is high, at ∼4–11 every minute (see Table 1), we can easily follow ionospheric variations toward the Crab Pulsar and thus, unlike many calibration pipelines, do not apply archival global ionosphere models such as the ionosphere vertical total electron content (TEC) maps from NASA's Crustal Dynamic Data Information System (CDDIS)[15] to the pulsar. We thus avoid uncertainties associated with the coarse resolution of the TEC maps (5° in longitude by 2.°5 in latitude and 2 hr temporal resolution), the accuracy of ∼2–8 TECU, and modeling assumptions required in using it (in CASA, that the ionosphere is a thin shell at a constant height of 450 km). Indeed, unreliable TEC information can sometimes produce negative parallaxes with smaller errors (e.g., Deller et al. 2009), and recent analysis by Petrov (2023) found that while TEC maps certainly can help improve measurements, corrections to the default values and implementation were needed to obtain the best absolute astrometry.

Still, even for our close in-beam reference source, the ionospheric contributions will differ slightly between it and the Crab Pulsar. Thus, while for our main analysis described below we do not use the TEC maps, we describe a separate analysis applying a relative correction based on them in the Appendix. We find that this gives consistent astrometric results with those of Section 4 below.

For bandpass calibration (i.e., time-independent frequency calibration), we again use our giant pulses, this time creating visibilities (for details, see Lin et al. 2023), which we then averaged across time to solve for the complex bandpass. As before, we use Effelsberg as our reference antenna. The complex bandpass was smoothed with a median filter to remove any remaining RFI contributions, then modeled with a simple cubic spline interpolation and normalized to unity to preserve the flux density scale. We wrote our solutions to CASA compatible bandpass tables and applied the corrections to both the Crab Pulsar and the candidate in-beam source visibility sets generated by SFXC. We show a typical bandpass solution in Figure 3.

To verify our solutions, we also determined bandpass solutions using CASA's `bandpass` task on the calibrator sources (using Effelsberg as the reference antenna). We found that there were no significant differences between these solutions and those determined from the giant pulses. Since we do not use the calibrators elsewhere in our analysis, we decided to stick with the giant-pulse bandpass solutions.

Lastly, we used CASA's `gaincal` task with a solution interval of ∼5 minutes to refine our amplitudes on the gated Crab Pulsar visibilities. Overall, we find that this final amplitude correction showed no variations related to scintillation as in Deller et al. (2009), as expected given that the Crab Pulsar's scintillation decorrelation bandwidth is much smaller that the width of our sub-bands. As before, this adjustment to the absolute flux density scaling should not affect positions (which we confirmed by omitting this step), but does improve the S/N of images slightly, by $\lesssim$5%. We again apply these solutions to both the Crab Pulsar and candidate reference sources.

After calibration, we reduced the data to a more manageable size by lowering the spectral resolution to 1024 channels and the temporal resolution to 2 s.

3.3. Images

All imaging was done using CASA's `tclean` task. For all sources, we started with our full bandwidth, and used natural weighting to optimize S/N. The synthesized beam is similar in

[14] http://old.evlbi.org/user_guide/EVNstatus.txt

[15] https://cddis.nasa.gov/Data_and_Derived_Products/GNSS/atmospheric_products.html#iono

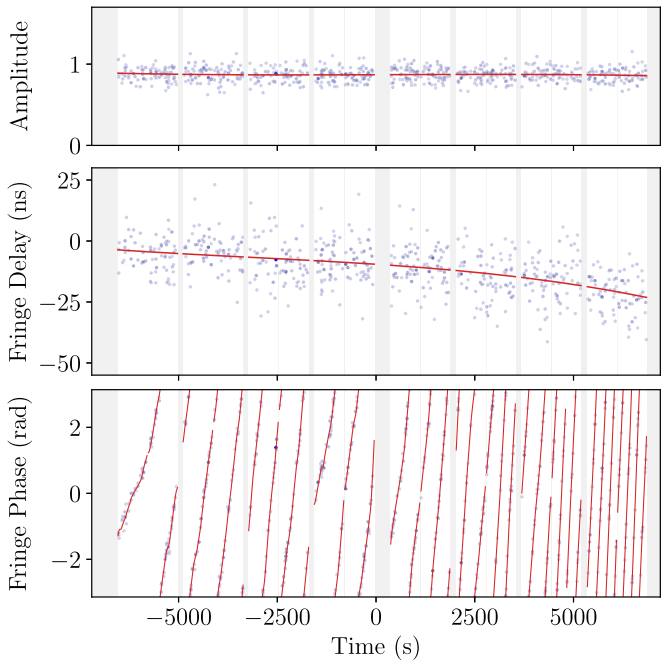

Figure 2. Amplitude (top), fringe delay (middle), and fringe phase (bottom) of Badary relative to Effelsberg derived from giant pulses of EK036 A for the frequency band 1626.49–1642.49 MHz in left-circular polarization (blue points). The opacity of the individual blue points scales with the square root of the S/N of the giant pulse. The red lines shows our fits. The gray shaded regions indicate when the telescope was not observing the Crab Pulsar. The fringe rate increases strongly near the end as the Crab Pulsar is setting at Badary.

all observations, with fan FWHM of roughly 4 mas × 12 mas, elongated in decl. To adequately sample this beam, we use a pixel size of 0.5 mas for our images. All of our generated images are 4096 × 4096 pixels in size.

We first formed dirty images for all of our visibility sets. For the Crab Pulsar, after applying the initial calibrations to the visibilities, we applied further calibrations in two separate ways: one using only solutions inferred from the calibrator sources (i.e., phase-referencing), and one using the solutions obtained from giant pulses (i.e., self-calibration). We compare the resulting dirty images of the Crab Pulsar in Figure 4. One sees that our giant pulse self-calibration provides much better results. Thus, for the candidate reference sources, after applying the initial calibrations, we applied further calibrations using only solutions obtained from giant pulses (i.e., effectively phase-referenced relative to the Crab Pulsar).

From these dirty images, we were only able to confidently see two of the in-beam candidate sources, SE_CAND3 and NE_CAND4. This is perhaps unsurprising, since the other candidate sources are much weaker (see Table 3), and our average sensitivity limit is quite poor: even away from the nebula, the rms is ∼0.25 mJy beam^{-1}. Another possibility is that some of these sources are extended beyond our largest angular scales (∼140 mas) and hence resolved out.

For SE_CAND3, we measured fluxes between ∼13 and 24 mJy in our four epochs, while for NE_CAND4, we found fluxes between ∼3 and 5 mJy. For comparison, for SE_CAND3, Petrov (2021) gave 4.3 and 7.6 GHz fluxes of ∼42 and ∼36 mJy, respectively, in the WFCS, while Gordon et al. (2021) found 3 GHz fluxes of ∼39 and ∼4 mJy in VLASS for SE_CAND3 and NE_CAND4, respectively. These fluxes seem roughly consistent, taking into account our approximate flux calibration,

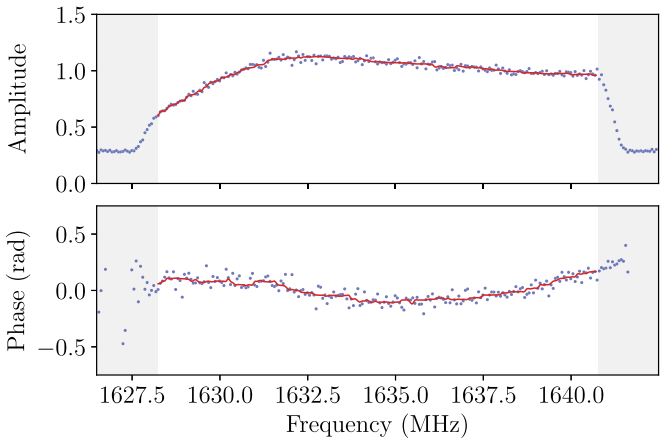

Figure 3. Complex bandpass amplitude (top) and phase (bottom) of Lovell relative to Effelsberg derived from giant pulses of EK036 A for the frequency band 1626.49–1642.49 MHz in left-circular polarization (blue points). The red lines shows our fits. The gray shaded regions indicate where we flagged data in CASA, as little signal is detected and the passband rolls off.

differences in observing frequency and resolution, as well as possible source variability and structure.

The positions of SE_CAND3 and NE_CAND4 are within 50 mas of their correlation centers (see Figure 5) and well within the uncertainties of positions measured in the VLA data. Thus, phase drifts resulting from the sources not being exactly at their correlation center are negligible (Fomalont et al. 1999), and we do not re-correlate any data.

To clean our images of the Crab Pulsar, SE_CAND3, and NE_CAND4, we apply a single elliptical mask the size and orientation of the synthesized beam centered on the peak flux in the dirty images to guide the cleaning. The cleaning was stopped when the residual reached an rms equal to that of a 4096 × 4096 pixel dirty map centered ∼2″ west from the source (this is far enough away that there are no sources in the map, and side-lobe effects do not affect the field significantly so the average rms measurement is more accurate; the noise level was measured using CASA's `imstat` task).

We show our clean images of the Crab Pulsar and the two in-beam candidates SE_CAND3 and NE_CAND4 in Figure 5. Since we self-calibrated on the pulsar, its position is fixed to the antenna pointing position (see Table 2). Assuming an extragalactic origin of the in-beam candidate sources, one expects them to move slightly between epochs. As can be seen in Figure 5, this is indeed the case.

3.4. Positions and Their Uncertainties

We first tried fitting the cleaned source images with elliptical Gaussians using the CASA task `imfit`, which is based on the procedure of Condon (1997). However, we found that the position errors provided by `imfit` were odd—we expected errors in R.A. and decl. to scale with their respective beam sizes, but found that the ratio was substantially different (with errors in decl. a factor 7–10 times larger than those in R.A., instead of the expected factor of ∼3). We compared CASA's `imfit` results with those from the `jmfit` task from the Astronomical Image Processing System (AIPS; Associated Universities 1999), which is also based on Condon (1997). The fitted positions were consistent, but the uncertainties from AIPS's `jmfit` do have the expected scaling with beam size.

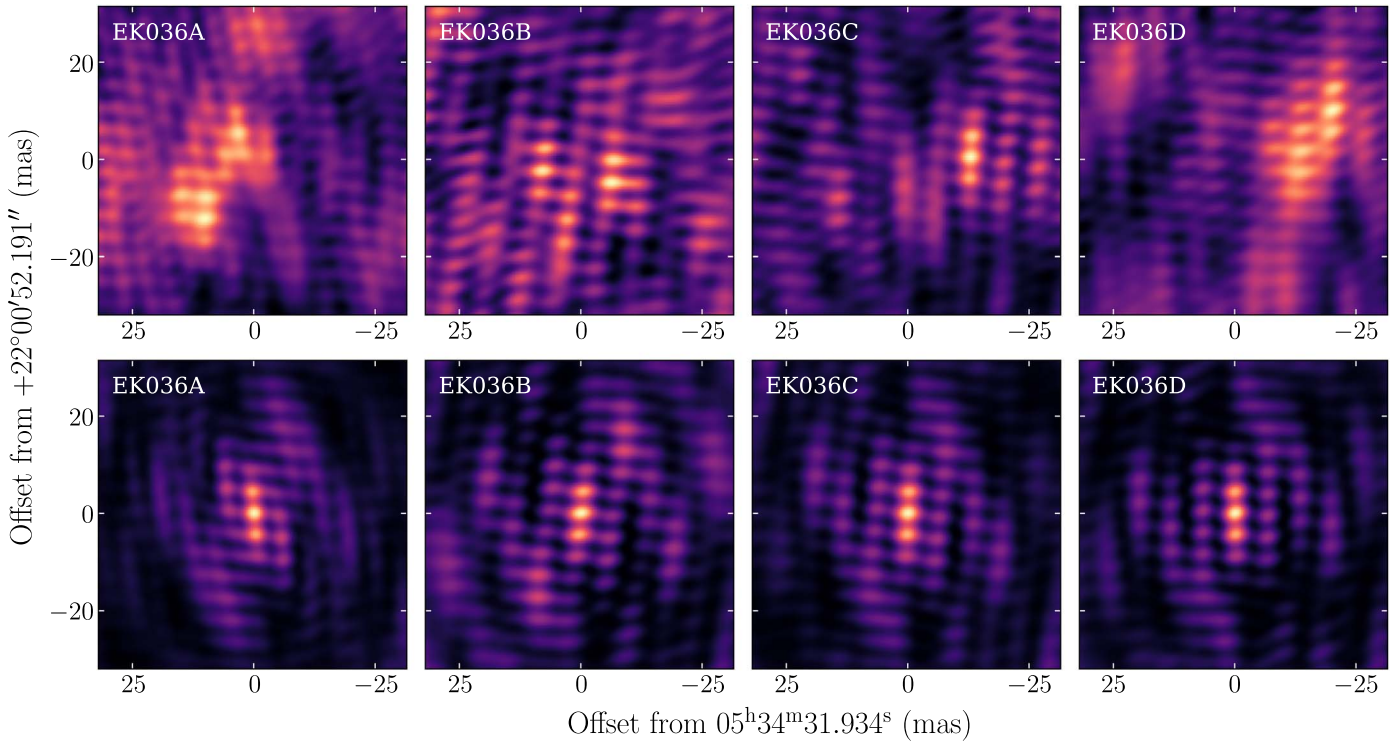

Figure 4. Dirty images of the Crab Pulsar for our four observations, comparing calibration solutions transferred from calibrator sources with those using giant pulses for self-calibration. Top: in general, transfer of the calibrator solutions to the Crab Pulsar resulted in poor images, particularly for EK036 A and EK036 B where the calibrator/target cycle was ∼0.5/25 minutes and ionospheric variations could not be modeled well. In EK036 C and EK036 D, the calibrator/target cycle was ∼1/5 minutes resulting in somewhat better dirty images. Bottom: using calibration solutions derived directly from the Crab Pulsar's giant pulses significantly improves the dirty images, with the Crab Pulsar clearly located in the center.

To investigate this discrepancy in position uncertainties, we implemented our own elliptical Gaussian fit routine in PYTHON. We discovered that the discrepancy between CASA and AIPS comes from how the noise and restoring beams are used when determining S/N. We concluded that for a point source, the procedure of AIPS's `jmfit` task is the logical one: calculate the S/N from the ratio of fitted peak amplitude and measured rms, and then estimate position uncertainties as usual for correlated noise, by dividing the fitted beam sizes by the S/N, and rotate to R.A. and decl. (in our case, the beam is nearly aligned, so the effects of rotation are tiny).

To derive our final positions, we used our fitting routine, taking a large 128×128 pixel window centered on the peak of each image to ensure a good fit. The rms fluctuations were measured from the whole image with the 128×128 pixel window centered on the peak removed. We confirmed that our fitted positions were in agreement with those from CASA and AIPS and our errors were consistent with those from AIPS, but different from those of CASA[16]

From Figure 1, we see that both SE_CAND3 and NE_CAND4 are outside the FWHM of the Effelsberg beam. To confirm that we have applied our primary beam corrections correctly and Effelsberg does not affect the positions of the candidate sources, we remove visibilities with baselines involving Effelsberg and verified that the positions remain unchanged. As all images are calibrated to the pulsar, the positions are relative to it, and thus the inferred position of the pulsar should by definition be equal to the pointing center. We confirmed that this was indeed the case (to well within nominal uncertainties) by fitting the Crab Pulsar's cleaned images as well.

The position uncertainties calculated this way may be slightly underestimated, since we are fitting a zero level offset instead of fixing one, and errors made in cleaning our images may not have fully propagated. In addition, errors from EK036 B-D may be underestimated a bit more than those of EK036 A because of their sparser coverage of the *uv*-plane (EK036 A was twice as long as the other epochs, and more EVN stations participated in the observation). Finally, beyond fitting errors, there could be other residual cleaning artifacts, as well as unmodeled ionospheric and instrumental effects.

To estimate such errors for each epoch individually ("intra-epoch error"), we compare the position offsets of SE_CAND3 inferred from the full bandwidth with offsets measured across spectral windows (similar to Deller et al. 2009; we omitted NE_CAND4 as its S/N in the images from the whole bands was already rather poor). For this purpose, we made cleaned images of the sources by splitting the total bandwidth into four, 32 MHz–wide parts, and fitted those to infer positions.[17] To account for this additional source of uncertainty, we added intra-epoch errors for SE_CAND3 by the amount, added in quadrature to each relative position measurement in an epoch, required to produce a $\chi^2_{\rm red} = 1$ (separately for right accession and decl.; see Table 4). This is a somewhat more conservative approach than simply scaling the errors to obtain a $\chi^2_{\rm red} = 1$, but ignores that with only four measurements there is a reasonable probability to find either smaller or larger $\chi^2_{\rm red}$

[16] Our final parallax value and uncertainty do not change if we use the CASA uncertainties, since the differences in the error estimates end up being absorbed by the intra-epoch errors we add later.

[17] We tried making images for every spectral window (i.e., eight 16 MHz bands) but found the S/N to be too low for reliable position measurements.

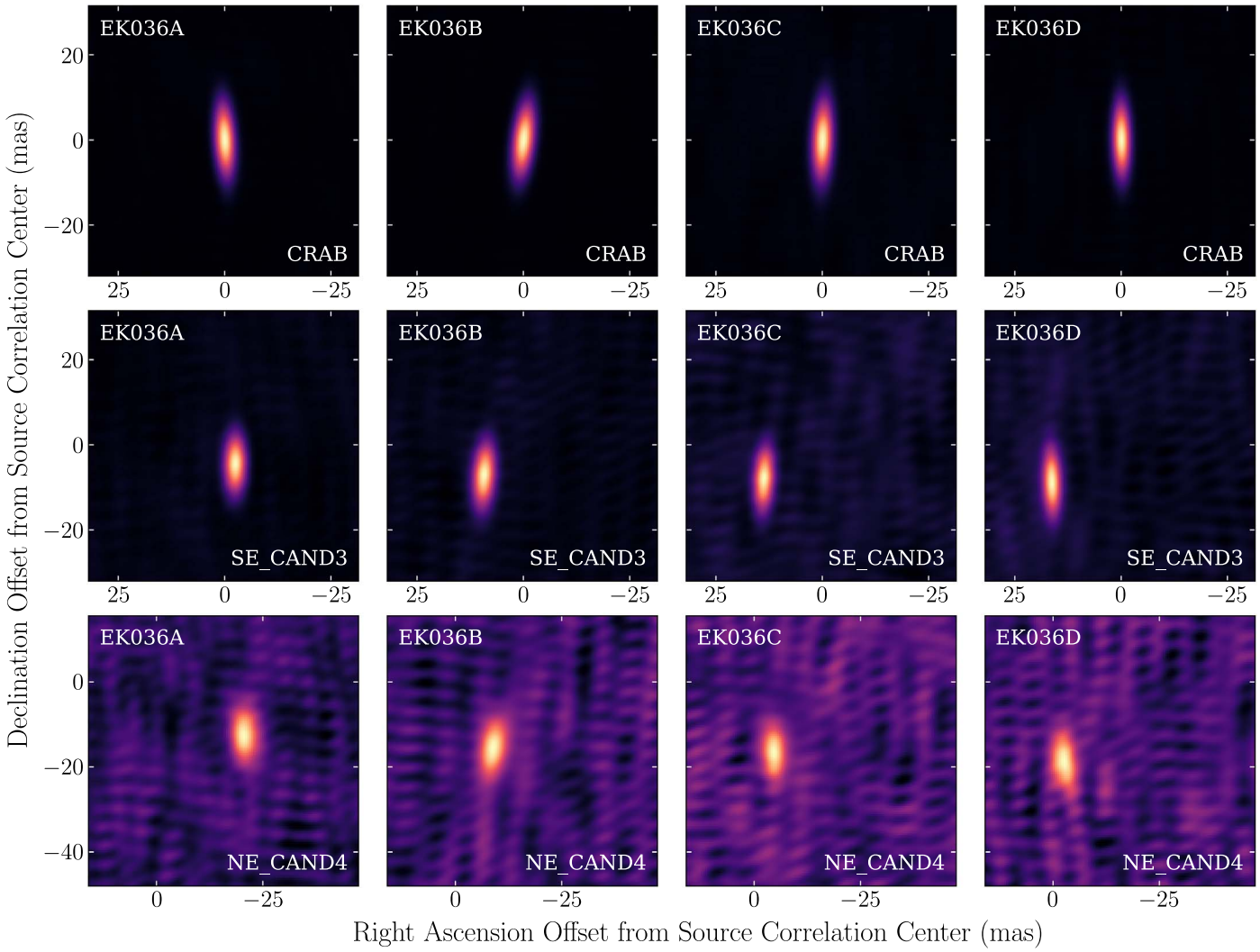

Figure 5. Clean images of the Crab Pulsar and candidate reference sources SE_CAND3 and NE_CAND4. The correlation centers for the pulsar are at the origin by construction. The centers for the other two are relative to those of the pulsar, and thus these sources show reflex motion (for details, see Section 3.1).

Table 4
Relative Positions between the Reference Sources and the Crab Pulsar

Observation Code	SE_CAND3		NE_CAND4	
	$\Delta\alpha^*$ (mas)	$\Delta\delta$ (mas)	$\Delta\alpha^*$ (mas)	$\Delta\delta$ (mas)
EK036 A	$-478472.866 \pm 0.013 \pm 0.00 \pm 0.04$	$243085.54 \pm 0.04 \pm 0.07 \pm 0.14$	-585690.43 ± 0.13	-195268.6 ± 0.3
EK036 B	$-478484.651 \pm 0.02 \pm 0.02 \pm 0.04$	$243088.25 \pm 0.06 \pm 0.14 \pm 0.14$	-585702.27 ± 0.2	-195265.4 ± 0.5
EK036 C	$-478489.143 \pm 0.03 \pm 0.03 \pm 0.04$	$243089.04 \pm 0.09 \pm 0.11 \pm 0.14$	-585706.66 ± 0.18	-195264.3 ± 0.4
EK036 D	$-478491.763 \pm 0.02 \pm 0.03 \pm 0.04$	$243089.84 \pm 0.09 \pm 0.09 \pm 0.14$	-585708.76 ± 0.19	-195262.1 ± 0.5

Note. All R.A. offsets are calculated at the decl. of the pulsar. For SE_CAND3, we provide the measurement errors inferred from the fits to the cleaned images, and estimates of the intra-epoch (see Section 3.4) and inter-epoch errors (see Section 4), respectively. These should be added in quadrature to obtain the total uncertainty. For NE_CAND4, we list only the errors from the position fit, since they are substantially larger than any systematic effects.

values by chance. It would be worthwhile to explore this further for a larger data set.

In order to check the effect of duration, we also tried splitting the EK036 A observation in half, such that the duration and *uv* coverage are similar to what we have in our other observations. We find that the intra-epoch errors in both halves of the EK036 A observation increase and become comparable to those in the other observations, suggesting that increased sampling in the *uv*-plane helps minimize systematic errors.

Our final adopted positions and the associated uncertainties are listed in Table 4.

4. Astrometry

We use the position offsets from Table 4 to fit for the parallax (π), proper motion (μ_{α^*}, μ_δ)[18] in R.A. and decl., respectively, and residual positional offset ($\Delta\alpha_0^*$, $\Delta\delta_0$), again in

[18] We denote differences in R.A. multiplied by $\cos\delta$ with *.

Table 5
Astrometric Parameters

Parameter	EVN	Gaia DR3
π (mas)…	0.53 ± 0.06	0.51 ± 0.08
μ_{α^*} (mas yr^{-1})…	-11.34 ± 0.06	-11.51 ± 0.10
μ_δ (mas yr^{-1})…	2.65 ± 0.14	2.30 ± 0.06
α_{J2000}…	$5^h34^m31\overset{s}{.}93357$	$5^h34^m31\overset{s}{.}933561(5)$
δ_{J2000}…	22°00′52.″1927	22°00′52.″19236(6)
d (kpc)…	$1.90^{+0.22}_{-0.18}$	$1.96^{+0.36}_{-0.26}$
$v_\perp$ (km s^{-1})…	104^{+13}_{-11}	109^{+21}_{-15}

Note. Shown are both our results and those from Gaia. Distances are calculated directly from the parallax measurements, and the transverse velocity $v_\perp$ is inferred from the proper motion and inferred distance. Coordinates listed here are in the J2000 ICRS frame at MJD 57680 (our reference epoch), with the uncertainties in our EVN results dominated by the uncertainty in the position of our reference source (∼1 mas, see the text), and those for Gaia given by the values in parentheses.

R.A. and decl., respectively. In terms of these parameters, the observed offsets are fit to,

$$\Delta\alpha_i^* = \pi f_{\alpha^*,i} + \mu_{\alpha^*}(t_i - t_0) + \Delta\alpha_0^*,$$
$$\Delta\delta_i = \pi f_{\delta,i} + \mu_\delta(t_i - t_0) + \Delta\delta_0, \quad (1)$$

where t_0 is a reference time—which we chose to be the average time over our observations (MJD 57680) to minimize covariance between the proper motion and the position offsets—and f_{α^*} and f_δ are the parallax factors, given by

$$f_{\alpha^*}(t) = X(t)\sin(\alpha_0) - Y(t)\cos(\alpha_0), \quad (2)$$

$$f_\delta(t) = [X(t)\cos(\alpha_0) + Y(t)\sin(\alpha_0)]\sin(\delta_0) - Z(t)\cos(\delta_0), \quad (3)$$

where $X(t)$, $Y(t)$, and $Z(t)$ are the components of the barycentric position of the Earth at time t, and α_0 and δ_0 are the approximate position of the Crab Pulsar (i.e., we neglect differences between the precise and approximate positions of the Crab Pulsar in the sine and cosine terms). We use ASTROPY (Astropy Collaboration et al. 2013, 2018, 2022) to calculate the barycentric positions.

As mentioned in Section 2, SE_CAND3 is identified also in the VLBA calibrator survey and is likely an active galactic nucleus. We compared the differences in relative positions of SE_CAND3 and NE_CAND4 between the epochs. We found these to be roughly consistent with zero and thus conclude NE_CAND4 likely also is extragalactic in origin. As NE_CAND4 is much weaker than SE_CAND3 and its position measurements are much less reliable, we will only use SE_CAND3 in our parallax and proper-motion fits below.

Our preliminary fit, including intra-epoch errors (see Section 3.4 and Table 4), yielded a parallax $\pi = 0.54 \pm 0.03$ mas and proper motion of $(\mu_{\alpha^*}, \mu_\delta) = (-11.31 \pm 0.03, 2.65 \pm 0.08)$ mas yr^{-1}. We find $\chi^2_{\rm red} = 2.3$, larger than the expected unity. This could simply reflect that we have very few degrees of freedom: in particular, the parallax fit is dominated by the four R.A. offsets, to which three parameters are fitted, leaving only a single degree of freedom. Indeed, Reid et al. (2017) showed that with four epochs and one effective degree of freedom, the uncertainty in the parallax can be significant. Still, we will assume conservatively that, instead, there are unmodeled systematic errors between epochs ("inter-epoch errors"). We estimate these at 0.04 mas and 0.14 mas, for right accession and decl., respectively, the value that, added in quadrature to the measurement errors of both R.A. and decl. in all epochs, gives a $\chi^2_{\rm red} = 1$ (see Table 4). The inter-epoch errors in R.A. and decl. were taken to be roughly proportional to the beam size, as might be expected if the systematic effects are due to phasing errors.[19] With these, we derive the final fit results presented in Table 5 and shown in Figures 6 and 7.

We also split the EK036 A observation in half in time and use the source position fits obtained from each half as independent measurements in a new fit for the parallax and proper motion. We find no significant changes in our fit parameters; however, the error on the parallax reduces a little, and there is less of a need for an inter-epoch contribution. Since this may just be a statistical fluke, we continue with our regular solution below.

One possible cause of systematic errors between epochs might be residual ionospheric errors between the pulsar and SE_CAND3. To give a sense of the size of the error from differences between the mean path length through the ionosphere, we find from CDDIS TEC maps that the average residual vertical TEC between antennas for SE_CAND3 relative to the pulsar is ∼0.02 TECU. Though the resolution and accuracy of the TEC maps are poor, if we take the residual vertical TEC at face value, this translates to an extra path length of ∼0.3 cm, which, if systematic over all telescopes, might induce position offsets of up to ∼0.06 mas, comparable to the inter-epoch errors we infer. Indeed, in the Appendix, we show that the inclusion of residual ionosphere correction from TEC map information results in shifts in position of this order of magnitude. We also find this leads to somewhat smaller inferred inter-epoch error and thus smaller uncertainties in the astrometric parameters, but do not feel confident enough in these results to use them (see the Appendix).

Another source of systematic error may come from refraction in the interstellar medium. This will affect both the calibrators and the pulsar, but differently. For an estimate, we use that Rudnitskii et al. (2016) measured a scattering disk with FWHM varying between 0.5 and 1.3 mas at 18 cm. The variability suggests that at times the screen is asymmetric, which would lead to position offsets if not accounted for. If this induces relative position shifts of the order of 10% of the width, which seems not unreasonable, it would induce offsets of ∼0.05 mas, the right order of magnitude to account for the possible systematic errors between epochs.

Finally, in our source images we see no apparent jets or other structures that could induce positional errors. However, we note that Koryukova et al. (2022) found that for SE_CAND3, the measured angular core size appeared to vary between ∼0.07 and 1.56 mas at 4–8 GHz for two observations separated by 2.6 yr. If real, this variability might also change the centroid by amounts comparable to the systematic errors we infer between epochs.

[19] Our results suggest the error in decl. may be overestimated. If we take errors that are the same in each coordinate, we find we require these to be 0.04 mas. With these, we find identical results except for a somewhat reduced final error in the proper motion in decl.

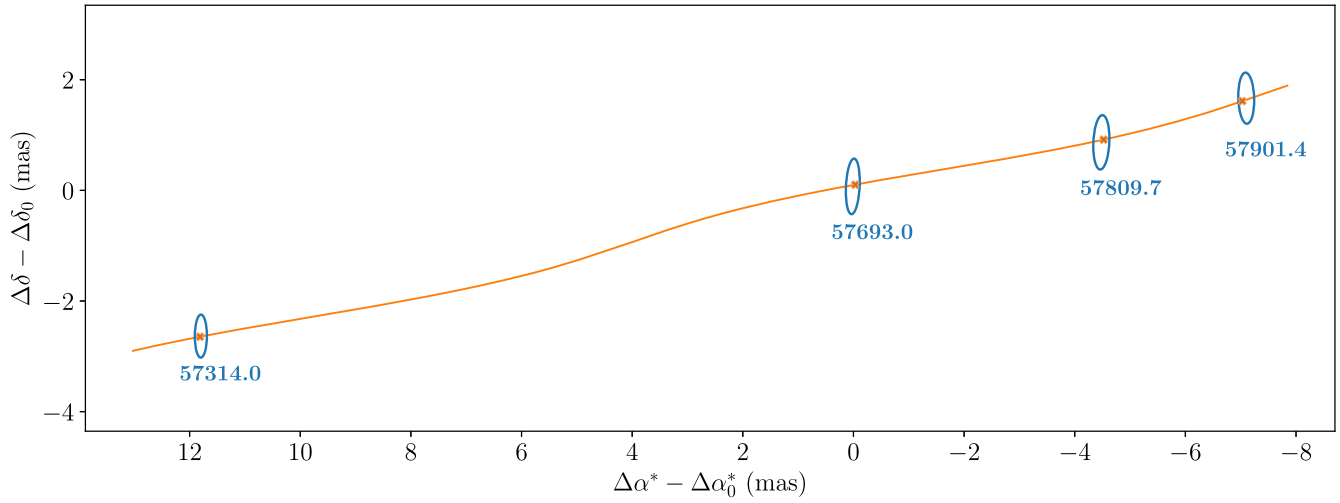

Figure 6. Motion of the Crab Pulsar on the sky. Shown are 95.4% confidence ellipses (in blue) of our four position offsets between the Crab Pulsar and SE_CAND3 (see Table 4), after subtracting the best-fit offset at our reference epoch, MJD 57680 (see Table 5). The modeled trajectory of the Crab Pulsar based our best-fit astrometry (see Table 5) is shown by the orange line, with the orange crosses corresponding to the modeled positions at the times of our four observations.

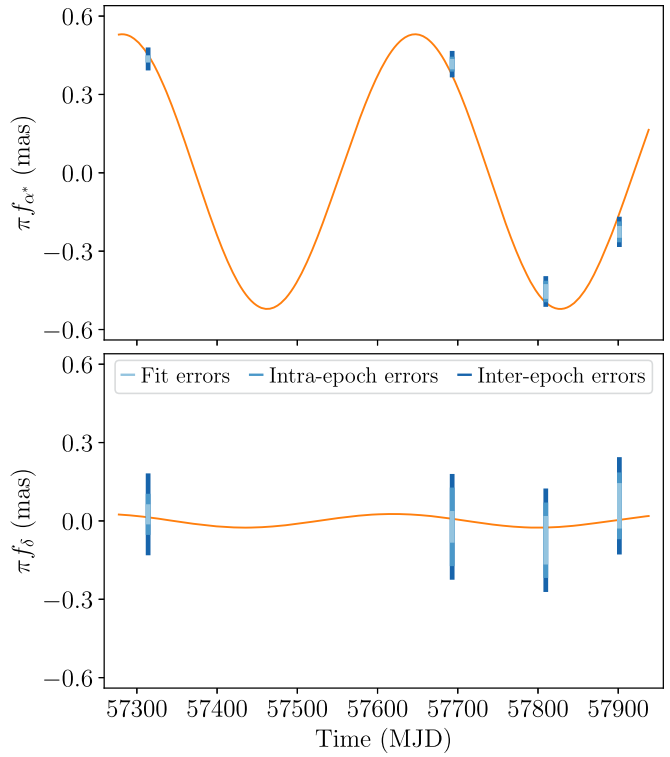

Figure 7. Position residuals in R.A. (top) and decl. (bottom). The best-fit proper motion and relative offset between the Crab Pulsar and SE_CAND3 have been removed, leaving just the signal due to parallax. Different colors in the error bars indicate the effects of the additional contributions to the uncertainties (see Table 4).

5. Results

We measure a parallax of $\pi = 0.53 \pm 0.06$ mas for the Crab Pulsar and infer a distance of $d = 1.90^{+0.22}_{-0.18}$ by taking the reciprocal of the measured parallax (we do not attempt to correct for Lutz & Kelker 1973 bias, as it is not clear what the prior likelihood of finding a supernova remnant at a given height above the galactic plane would be). From our best-fit proper motion and inferred distance, we also derive a transverse velocity of $v_\perp = 104^{+13}_{-11}$ km s^{-1}. Using the coordinates of SE_CAND3 (WFCS J0535+2156; Petrov 2021),

$$\alpha_{\rm J2000} = 5^{\rm h}35^{\rm m}06\overset{\rm s}{.}34125,$$
$$\delta_{\rm J2000} = 21°56'49\overset{''}{.}1045, \quad (4)$$

in the J2000 International Celestial Reference System (ICRS) frame, we determine the absolute position of the Crab Pulsar, in the same reference frame, at MJD 57680, as,

$$\alpha_{\rm J2000} = 5^{\rm h}34^{\rm m}31\overset{\rm s}{.}93357,$$
$$\delta_{\rm J2000} = 22°00'52\overset{''}{.}1927. \quad (5)$$

The uncertainty in our position for the Crab Pulsar is dominated by the uncertainty in the position of SE_CAND3. The formal errors are ±0.6 mas in each coordinate, but those are for the positions measured at 4–8 GHz, and we have not accounted for possible frequency dependent core-shifts, which typically are of the order of 1 mas (Sokolovsky et al. 2011). Hence, we estimate the uncertainties in the position at ∼1 mas in each coordinate. Our measured and derived values are presented in Table 5.

Comparing our results with those of Gaia DR3, listed also in Table 5, we find good agreement for the parallax but some tension for the proper motion. To investigate this further, we show confidence ellipses of our parallax and proper motion along with those from Gaia DR3 in Figure 8. One sees that the main discrepancy is for the proper motion in decl. Our measurements are less sensitive in decl., since most EVN telescopes are spread east–west, with most of the north–south constraint coming from Hartebeesthoek. Thus, we may still underestimate the uncertainty of the proper motion in decl. Fortunately, this should not affect the parallax: since the Crab Pulsar is near the ecliptic, the parallax barely correlates with the proper motion in decl. It has some correlation with proper motion in R.A., and, taking our error ellipse and that of Gaia DR3 at face value, a slightly lower parallax might be inferred.

We note that systematic effects may affect not just our measurement (see above), but also the Gaia DR3 astrometry of the Crab Pulsar. Indeed, the values for the proper motion presented in Gaia DR2 and DR3 differ significantly (see Section 1). For the parallax, there is a possible overall zero-point correction, but this is a small effect: applying the

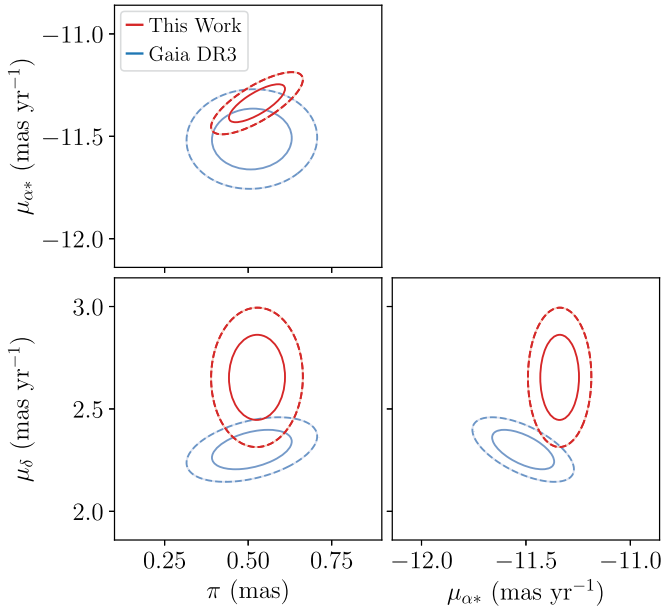

Figure 8. Error ellipses of the parallax and proper motion from our work (in red) and Gaia DR3 (in blue). The 68.3% and 95.4% confidence ellipses are shown by the solid and dashed ellipses, respectively.

correction of −0.03 mas from Lindegren et al. (2021a) to the raw Gaia DR3 parallax from Table 5 yields $\pi = 0.54 \pm 0.08$ mas (and an inferred distance of $d = 1.86^{+0.32}_{-0.24}$), which still agrees well with our measured and inferred results. Another possible systematic effect is due to source color. In Gaia DR3, a six-parameter fit including the pseudo-color was used for the astrometry, and the solution shows fairly strong covariance between the pseudo-color and the proper motion. According to Lindegren et al. (2021b), for cases where strong correlation is seen, independent color information may significantly improve precision and accuracy. Here, one would have to be somewhat careful, since the Crab Pulsar's spectrum is not like that of regular stars, for which the color corrections are calibrated. Finally, it also seems possible that the variable optical emission surrounding the Crab Pulsar, such as the wisp-like structures moving outward from the pulsar, and halos and knots close to it (Hester et al. 2002; Tziamtzis et al. 2009), might induce positional offsets that could affect the astrometry. We conclude that in both optical and radio it will be useful to analyze further observations and try to carefully account for potential biases and systematic effects.

6. Future Work

Our pilot study shows that it is possible to measure the parallax of the Crab Pulsar with VLBI. It should be relatively straightforward to improve the measurement down to the $\lesssim$5% level with further VLBI observations. The EVN's extended east–west baseline is particularly useful for constraining the parallax of the Crab Pulsar, as the synthesized beam is narrower in R.A. and the pulsar is very close to the ecliptic. More observations should be scheduled around October and March when the parallax signature would peak in R.A..

Future observations should try to include more small dishes to give maximum sensitivity for the in-beam extragalactic reference sources. Furthermore, the pointing center can be shifted toward SE_CAND3 and NE_CAND4 (e.g., centroid of all sources) to boost the signal of those sources. With the higher sensitivity, NE_CAND4 should become more useful in helping to constrain and verify the astrometry. The addition of NE_CAND4 may also allow one to use the MultiView technique (Rioja et al. 2017), or variants thereof (e.g., Reid et al. 2017; Hyland et al. 2022), which has shown success in improving residual spatial ionospheric corrections.

We have shown that our technique of using giant pulses to determine fringe and bandpass solutions works exceedingly well for self-calibration, removing the need to observe phase calibrators. Our estimates of systematic effects between epochs suggests it is better to have a larger number of observations rather than to have longer ones. However, since the intra-epoch error for EK036 A is quite a bit smaller than in EK036 B-D, one would not want to reduce the time too much.

With more observations and better time coverage, the error analysis could be improved, e.g., using a bootstrap fit like was done by Deller et al. (2019). Overall, we suggest at least eight to nine observations, each lasting at least 2 hr in order to ensure sufficient *uv* coverage. If the detection rate of strong giant pulses remain high enough for self-calibration, it may be better to observe at slightly higher frequencies, say ∼2 GHz, to reduce the effects of ionospheric variations and interstellar scattering. Calibration of both scattering and residual ionospheric effects would be helped by simultaneous dual-frequency or wide-band ($\gtrsim$350 MHz) observations (Brisken et al. 2000; Petrov 2023). These wider-band observations may allow for an alternative measurement of the small differences in contributions from the ionosphere between the Crab Pulsar and the in-beam calibrators and improve on the application of TEC maps described in the Appendix. Of course, ionospheric errors can also be reduced by trying to schedule observations when the solar cycle is at its minimum.

Our technique of self-calibration using giant pulses should also help future studies of the Crab Pulsar's environment, such as the flaring regions within the Crab Nebula studied by Lobanov et al. (2011). Furthermore, the technique may also be useful for measuring distances to other giant pulse emitters such PSR J1824−2452A (Bilous et al. 2015) and PSR J1823−3021A (Abbate et al. 2020), as well as to bright rotating radio transients[20] such as PSR J1819−1458 and PSR J1840−1419, which have bursts every ∼3.4 min and ∼1.3 min, respectively (McLaughlin et al. 2006). For PSR J18242452A and PSR J1823-3021A, which are both in globular clusters, using their pulses for phase calibration would also aid searches of further globular cluster pulsars and other radio emitters. Similarly, applying our technique to the Crab Pulsar twin PSR J0540-6919, which also exhibits giant pulses (Geyer et al. 2021), may help searches of new radio sources in the Large Magellanic Cloud.

Our cleaned images in FITS format are made available as a data set at 10.5281/zenodo.7910778. The raw baseband data along with our custom scripts are available upon request.[21]

Acknowledgments

We thank Cees Bassa for his contribution to the EVN proposal and the anonymous referee for providing useful comments. R.L. thanks Aard Keimpena, Bob Campbell, Benito Marcote, and Marjolein Verkouter for useful advice on using SFXC and JIVE post-processing tools. R.L. thanks the National Radio Astronomy Observatory (NRAO) helpdesk for advice on

[20] http://astro.phys.wvu.edu/rratalog/

[21] As the baseband data were correlated by us and not by the JIVE team, the visibility products are not available on the EVN Data Archive.

using CASA, including details of the structure of the various tables, and for providing access to the NRAO computing facilities. Computations were performed on the New Mexico Array Science Center (NMASC) cluster and the Niagara supercomputer at the SciNet HPC Consortium (Loken et al. 2010; Ponce et al. 2019). SciNet is funded by: the Canada Foundation for Innovation; the Government of Ontario; Ontario Research Fund - Research Excellence; and the University of Toronto. M.Hv.K. is supported by the Natural Sciences and Engineering Research Council of Canada (NSERC) via discovery and accelerator grants, and by a Killam Fellowship. F.K. acknowledges support from the Onsala Space Observatory for the provisioning of its facilities/observational support. The Onsala Space Observatory national research infrastructure is funded through Swedish Research Council grant No. 2017-00648. U.-L.P. receives support from Ontario Research Fund-Research Excellence Program (ORF-RE), NSERC [funding reference Nos. RGPIN-2019-067, CRD 523638-18, 555585-20], Canadian Institute for Advanced Research (CIFAR), the National Science Foundation of China (grant No. 11929301), Alexander von Humboldt Foundation, and the National Science and Technology Council (NSTC) of Taiwan (111-2123-M-001, −008, and 111-2811-M-001, −040).

Facilities: The European VLBI Network is a joint facility of independent European, African, Asian, and North American radio astronomy institutes. Scientific results from data presented in this publication are derived from the following EVN project codes: EK036 A-D. The NRAO is a facility of the National Science Foundation operated under cooperative agreement by Associated Universities, Inc.

Software: astropy (Astropy Collaboration et al. 2013, 2018, 2022), Baseband (Van Kerkwijk et al. 2020), CALC10 (Ryan & Vandenberg 1980), CASA (The CASA Team et al. 2022), numpy (Harris et al. 2020), matplotlib (Hunter 2007), pulsarbat (Mahajan & Lin 2023), scipy (Gommers et al. 2022), SFXC (Keimpema et al. 2015), tempo2 (Hobbs & Edwards 2012).

Appendix
Differential Ionosphere Corrections Using TEC Maps

A source of error in our position measurements of the Crab Pulsar relative to our in-beam calibrators arises from slight differences in the total electron column (TEC) in the ionosphere between the different sources. Estimates of these differences can be made from TEC maps, as is becoming common in VLBI astrometry. While this use of TEC maps, including the underlying assumptions about the ionosphere, have not been fully validated (see Petrov 2023), we follow it to get a sense of the improvement that may be attainable. Since our giant-pulse-based fringe solutions already include the contribution of the ionosphere toward the Crab Pulsar (along with delays introduced by antenna location, electronics, geometric models, etc.), we only need to apply a differential correction for the extragalactic sources.

To determine the residual ionospheric corrections, we first download CDDIS TEC maps using CASA's `tec_maps` function. We then use CASA's `gencal` task to estimate the line-of-sight TEC from each antenna to each of our sources across each observation (`gencal` models the ionosphere as a thin shell at a constant height of 450 km). Using custom scripts, we then calculate the differential TEC between the Crab Pulsar and extragalactic sources for each antenna and write the residuals into our own CASA compatible calibration tables. These new calibration tables are applied to the visibilities data of SE_CAND3 and NE_CAND4 using CASA's `applycal` task (after applying the calibrations described in Section 3.2). We then create images and extract position offsets as in Sections 3.3 and 3.4. We list the resulting offsets in Table A1, and fit these to our astrometric model (including intra- and inter-epoch errors estimated like in Sections 3.4 and 4).

We find a parallax of $\pi = 0.49 \pm 0.04$ mas and proper motion of $(\mu_\alpha,\ \mu_\delta) = (-11.41 \pm 0.05,\ 2.54 \pm 0.11)$ mas yr^{-1}, i.e., values consistent with our results in Section 5 and with Gaia DR3. We note that the uncertainties are slightly reduced, a consequence of the fit to the offsets being somewhat better, thus reducing the estimated inter-epoch error contribution to the uncertainties. While encouraging, we caution that with the small number of data points, a reduction by chance is not unlikely, in particular in the presence of possible other sources of systematic error such as refraction in the interstellar medium and source variability (see Section 4).

As a further check on the reliability, we also tried applying TEC corrections when transferring calibrator solutions to the pulsar as above, but this time applying a differential correction for the pulsar. As the angular separations of the calibrator sources and pulsar are quite large and the calibrator/pulsar cycle is quite long, we also tried removing the ionospheric contributions toward the calibrators using the TEC maps before solving for the calibrator fringes (in the hopes that these new calibrator fringe solutions with slower time variations can be better extrapolated to the pulsar). We then applied TEC corrections toward the Crab Pulsar and the new calibrator fringe solution to the pulsar. Both methods resulted in similar quality images. If the corrections were good, we expect that with these solutions, the dirty images would improve, i.e., that we would see the Crab Pulsar becoming more pointlike. However, we found that with the TEC corrections, the dirty images were of poorer quality (more smeared) than those shown in the top panels of Figure 4. Given this contradictory result, we concluded that without better understanding, it was best not to use the above TEC-map assisted astrometry, even

Table A1
Relative Positions between the Reference Sources and the Crab Pulsar, with Ionosphere Corrections Applied

Observation Code	…SE_CAND3 …		…NE_CAND4 …	
	$\Delta\alpha^*$ (mas)	$\Delta\delta$ (mas)	$\Delta\alpha^*$ (mas)	$\Delta\delta$ (mas)
EK036 A	$-478472.634 \pm 0.015 \pm 0.00 \pm 0.03$	$243085.61 \pm 0.04 \pm 0.08 \pm 0.09$	-585690.03 ± 0.14	-195268.3 ± 0.3
EK036 B	$-478484.582 \pm 0.02 \pm 0.02 \pm 0.03$	$243088.27 \pm 0.06 \pm 0.14 \pm 0.09$	-585702.12 ± 0.2	-195265.3 ± 0.5
EK036 C	$-478489.033 \pm 0.03 \pm 0.02 \pm 0.03$	$243088.92 \pm 0.09 \pm 0.10 \pm 0.09$	-585706.43 ± 0.18	-195264.2 ± 0.4
EK036 D	$-478491.501 \pm 0.02 \pm 0.03 \pm 0.03$	$243089.78 \pm 0.09 \pm 0.09 \pm 0.09$	-585708.26 ± 0.19	-195261.8 ± 0.5

Note. Values and uncertainties are the same as for Table 4, except that here they were derived from data for which we tried to correct for differential ionospheric effects using TEC maps.

though it gave notionally better results. Since our "ionosphere corrected" SE_CAND3 and NE_CAND4 images may still be useful for future astrometry of the Crab Pulsar, we provide these (along with those from Figure 5) at 10.5281/zenodo.7910778.

ORCID iDs

Rebecca Lin https://orcid.org/0000-0003-4530-4254
Marten H. van Kerkwijk https://orcid.org/0000-0002-5830-8505
Franz Kirsten https://orcid.org/0000-0001-6664-8668
Ue-Li Pen https://orcid.org/0000-0003-2155-9578
Adam T. Deller https://orcid.org/0000-0001-9434-3837

References

Abbate, F., Bailes, M., Buchner, S. J., et al. 2020, MNRAS, 498, 875
Antoniadis, J. 2020, RNAAS, 4, 223
Associated Universities, I. 1999, AIPS: Astronomical Image Processing System, Astrophysics Source Code Library, ascl:9911.003
Astropy Collaboration, Price-Whelan, A. M., Lim, P. L., et al. 2022, ApJ, 935, 167
Astropy Collaboration, Price-Whelan, A. M., Sipőcz, B. M., et al. 2018, AJ, 156, 123
Astropy Collaboration, Robitaille, T. P., Tollerud, E. P., et al. 2013, A&A, 558, A33
Bietenholz, M. F., Kassim, N., Frail, D. A., et al. 1997, ApJ, 490, 291
Bilous, A. V., Pennucci, T. T., Demorest, P., & Ransom, S. M. 2015, ApJ, 803, 83
Brisken, W. F., Benson, J. M., Beasley, A. J., et al. 2000, ApJ, 541, 959
Caraveo, P. A., & Mignani, R. P. 1999, A&A, 344, 367
Chatterjee, S., Brisken, W. F., Vlemmings, W. H. T., et al. 2009, ApJ, 698, 250
Condon, J. J. 1997, PASP, 109, 166
Cordes, J. M., & Lazio, T. J. W. 2002, arXiv:astro-ph/0207156
Cutri, R. M., et al. 2012, yCat, II/311
Deller, A. T., Goss, W. M., Brisken, W. F., et al. 2019, ApJ, 875, 100
Deller, A. T., Tingay, S. J., & Brisken, W. 2009, ApJ, 690, 198
Duyvendak, J. J. L. 1942, PASP, 54, 91
Eilek, J. A., & Hankins, T. H. 2016, JPlPh, 82, 635820302
Espinoza, C. M., Lyne, A. G., Stappers, B. W., & Kramer, M. 2011, MNRAS, 414, 1679
Fomalont, E. B., Goss, W. M., Beasley, A. J., & Chatterjee, S. 1999, AJ, 117, 3025
Gaia Collaboration, Brown, A. G. A., Vallenari, A., et al. 2018, A&A, 616, A1
Gaia Collaboration, Vallenari, A., Brown, A. G. A., et al. 2023, A&A, 674, A1
Geyer, M., Serylak, M., Abbate, F., et al. 2021, MNRAS, 505, 4468
Gommers, R., Virtanen, P., Burovski, E., et al. 2022, scipy/scipy: SciPy, 1.8.0, v1.8.0, Zenodo, doi:10.5281/zenodo.595738
Gordon, Y. A., Boyce, M. M., O'Dea, C. P., et al. 2021, ApJS, 255, 30
Harris, C. R., Millman, K. J., van der Walt, S. J., et al. 2020, Natur, 585, 357
Hester, J. J., Mori, K., Burrows, D., et al. 2002, ApJL, 577, L49
Hobbs, G., & Edwards, R. 2012, Tempo2: Pulsar Timing Package, Astrophysics Source Code Library, ascl:1210.015
Hunter, J. D. 2007, CSE, 9, 90
Hyland, L. J., Reid, M. J., Ellingsen, S. P., et al. 2022, ApJ, 932, 52
Kaplan, D. L., Chatterjee, S., Gaensler, B. M., & Anderson, J. 2008, ApJ, 677, 1201
Keimpema, A., Kettenis, M. M., Pogrebenko, S. V., et al. 2015, ExA, 39, 259
Koryukova, T. A., Pushkarev, A. B., Plavin, A. V., & Kovalev, Y. Y. 2022, MNRAS, 515, 1736
Lawrence, A., Warren, S. J., Almaini, O., et al. 2012, yCat, II/314
Lin, R., van Kerkwijk, M. H., Main, R., et al. 2023, ApJ, 945, 115
Lindegren, L., Bastian, U., Biermann, M., et al. 2021a, A&A, 649, A4
Lindegren, L., Klioner, S. A., Hernández, J., et al. 2021b, A&A, 649, A2
Lobanov, A. P., Horns, D., & Muxlow, T. W. B. 2011, A&A, 533, A10
Loken, C., Gruner, D., Groer, L., et al. 2010, JPhCS, 256, 012026
Lorimer, D. R., Yates, J. A., Lyne, A. G., & Gould, D. M. 1995, MNRAS, 273, 411
Lutz, T. E., & Kelker, D. H. 1973, PASP, 85, 573
Lyne, A. G., Pritchard, R. S., & Graham Smith, F. 1993, MNRAS, 265, 1003
Mahajan, N., & Lin, R. 2023, pulsarbat: PULSAR Baseband Analysis Tools, v0.0.9, Zenodo, doi:10.5281/zenodo.6934356
Mayall, N. U., & Oort, J. H. 1942, PASP, 54, 95
McLaughlin, M. A., Lyne, A. G., Lorimer, D. R., et al. 2006, Natur, 439, 817
Minkowski, R. 1970, PASP, 82, 470
Moffett, D. A., & Hankins, T. H. 1996, ApJ, 468, 779
Petrov, L. 2021, AJ, 161, 14
Petrov, L. 2023, AJ, 165, 183
Ponce, M., van Zon, R., Northrup, S., et al. 2019, arXiv:1907.13600
Reid, M. J., Brunthaler, A., Menten, K. M., et al. 2017, AJ, 154, 63
Rioja, M. J., Dodson, R., Orosz, G., Imai, H., & Frey, S. 2017, AJ, 153, 105
Rudnitskii, A. G., Karuppusamy, R., Popov, M. V., & Soglasnov, V. A. 2016, ARep, 60, 211
Ryan, J. W., & Vandenberg, N. R. 1980, BAAS, 12, 457
Shaw, B., Keith, M. J., Lyne, A. G., et al. 2021, MNRAS, 505, L6
Sokolovsky, K. V., Kovalev, Y. Y., Pushkarev, A. B., & Lobanov, A. P. 2011, A&A, 532, A38
The CASA Team, Bean, B., Bhatnagar, S., et al. 2022, arXiv:2210.02276
Trimble, V. 1973, PASP, 85, 579
Tziamtzis, A., Lundqvist, P., & Djupvik, A. A. 2009, A&A, 508, 221
Van Kerkwijk, M. H., Zhu, C. C., Guo, S. G., et al. 2020, mhvk/baseband, v4.0.3, Zenodo,10.5281/zenodo.4292543
Wyckoff, S., & Murray, C. A. 1977, MNRAS, 180, 717
Yao, J. M., Manchester, R. N., & Wang, N. 2017, ApJ, 835, 29